PAPER

The generation and transport of reactive nitrogen species from a low temperature atmospheric pressure air plasma source†

Q1

Aaron Dickenson,[a] Nikolay Britun,[b] Anton Nikiforov,[c] Christophe Leys,[c] Mohammad Hasan[a] and James Walsh (ID) *[a]

The reactive chemical species generated by non-equilibrium plasma under atmospheric pressure conditions are key enablers for many emerging applications spanning the fields of biomedicine, manufacturing and agriculture. Despite showing great application potential, insight in to the underpinning reactive species generation and transport mechanisms remains scarce. This contribution focuses on the spatiotemporal behaviour of reactive nitrogen species (RNS) created and transported by an atmospheric pressure air surface barrier discharge (SBD) using both laser induced fluorescence and particle imaging velocimetry measurements combined with experimentally validated numerical modelling. It was observed that highly reactive species such as N are confined to the discharge region while less reactive species such as NO, NO_2 and N_2O closely followed the induced flow. The concentration of key RNS was found to be in the 10–100 ppm range at a position of 25 mm downstream of the discharge region. A close agreement between the experimental and computational results was achieved and the findings provide a valuable insight in to the role of electrohydrodynamic forces in dictating the spatiotemporal distribution of reactive chemical species beyond the plasma generation region, which is ultimately a key contributor towards downstream treatment uniformity and application efficacy.

1. Introduction

Reactions initiated by non-thermal plasma in atmospheric pressure air lead to the generation of a mixture of reactive chemical species such as NO, O_3, OH, H_2O_2, and O_2^-. The ability to generate such species in air under ambient conditions using low cost equipment has led to an increasing interest into the possible applications of cold plasma devices in healthcare related areas such as microbial decontamination, wound healing and cancer therapy.[1,2] When selecting a particular plasma system for a given application, two key requirements must be met: [1] the operating conditions must favour the generation of reactive species that are of particular importance for the intended application; for example, NO is known to aid wound healing through stimulation of proliferation and migration of wound related skin cells, whereas O and OH are important antimicrobial agents necessary for efficient pathogen decontamination.[3–6] [2] The uniformity of the plasma source must be sufficient to provide an even dose of reactive species over a characteristic surface area on a downstream target.

Of all the possible atmospheric pressure plasma systems currently under consideration,[7–9] the surface barrier discharge (SBD) is one of the simplest to construct, operates in ambient air with little potential for arcing and is easily scaled to cover treat large areas.[10] A typical SBD employs two metallic electrodes adhered to either side of a dielectric surface, on application of a sufficiently high voltage, plasma forms in the region where the electric field is the highest which is typically at the electrode edges. Critically, in this scenario, the plasma is essentially confined to the surface of the dielectric material and does not directly interact with a downstream target, hence it is the transport of plasma generated reactive chemical species to the target that is the primary application enabler.

Several previous studies have focused on the generation of reactive chemical species from atmospheric pressure air SBD system using Fourier Transform Infrared Spectroscopy (FTIR) for characterisation and quantification.[11–13] While these studies provide a valuable insight in to the nature of the species

[a] Centre for Plasma Microbiology, Department of Electrical Engineering & Electronics, University of Liverpool, L69 3GJ, UK. E-mail: JLWalsh@liverpool.ac.uk
[b] Chimie des Interactions Plasma-Surface, University of Mons, Place du Parc 23, Mons, Belgium
[c] Department of Applied Physics, Ghent University, Sint-Pietersnieuwstraat 41, Technicum B4, 9000 Ghent, Belgium
† Electronic supplementary information (ESI) available. See DOI: 10.1039/c8cp05762a

This journal is © the Owner Societies 2018

Phys. Chem. Chem. Phys., 2018, **00**, 1–12 | 1

produced, the requirement of placing the SBD into a closed chamber to undertake the measurement precludes the ability to perform spatially resolved measurements. Furthermore, operation of an SBD in a closed volume dictates "batch reactor" like conditions which likely differ from those observed when an SBD is operated in free space, as is the case in many applications.

This study focuses on the generation and transport of reactive nitrogen species (RNS) using laser induced fluorescence (LIF) and particle imaging velocimetry (PIV) measurements combined with computational modelling to uncover the underpinning reaction pathways and physicochemical processes governing the species transport. Considering that LIF can provide spatially resolved density measurements of various reactive species with high temporal resolution, it is the ideal technique for determining the distribution of species as they are transported downstream of the SBD. Indeed, previous studies have demonstrated that LIF diagnostics have been successfully applied for the measurement of NO under atmospheric pressure conditions in both helium and argon plasma jets.[14-18]

The results have shown that the transport of chemical species beyond the plasma generation region is primarily driven by convection, arising from the presence of electrohydrodynamic (EHD) forces in the discharge.[19,20] To quantify the influence of convection on the spatial distribution of NO, PIV was used to measure the induced flow field under different plasma operating conditions. In addition, a 2D numerical model, validated using the experimental measurements, was used to determine the spatial distribution of other key RNS beyond the discharge region and uncover the chemical pathways leading to their generation and loss. The findings provide a valuable insight in to the role of EHD forces in dictating the spatial distribution of reactive chemical species beyond the plasma generation region, knowledge which can be used to guide the future development of plasma systems for healthcare related applications.

2. Experimental setup and methods

2.1 Low temperature plasma source

A schematic representation of the SBD used in this investigation is shown in Fig. 1, the electrode unit consisted of a quartz sheet of 2 mm thickness, serving as a dielectric material. Electrodes were attached either side of the quartz, made from 35 μm thick copper film. The powered electrode was configured as two parallel strips separated by a 15 mm gap, referred to as the discharge gap. The outer edges of the powered electrodes were insulated using Kapton tape to prevent plasma formation on electrode edges beyond the discharge gap.

The powered electrode was driven by a custom-made high-voltage source capable of producing a sinusoidal output at a frequency of 18 kHz. Two voltage amplitudes of 13 kV and 15 kV were considered in this study. The discharge current and voltage waveforms were measured using a Tektronix P6015A
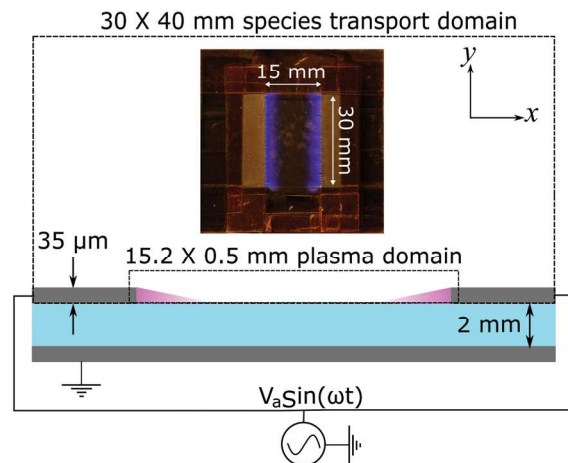

Fig. 1 Schematic showing cross-section of the surface barrier discharge used in both experimental and computational investigations (not to scale), insert shows birds eye view of discharge operating at an applied voltage of 15 kV.

high voltage probe and Pearson 2877 current monitor, recorded using a Tektronix DPO 5054 oscilloscope. Using the measured current and voltage waveforms, the dissipated power within the discharge was calculated and found to be 2.5 W and 4.3 W for the 13 kV and 15 kV cases, respectively. Using the calculated dissipated power at each applied voltage, estimated power densities of 4.67 kW m^{-2} and 8 kW m^{-2} were determined by dividing the measured power by the area covered by the visible plasma, which was estimated from photographs of the discharge operating at each applied voltage condition; these two cases will be referred to as the low power and high power cases, respectively. Fig. 1 also shows the computational domains for both the plasma module and the reactive flow module, described in Section 2.4.

2.2 Laser induced fluorescence setup

The LIF measurement system is shown in Fig. 2(a). A dye laser (Sirah Cobra Stretch with second harmonic generation (SHG) unit) was pumped by a 5 ns pulsed Nd:YAG laser with a wavelength of 355 nm at a repetition rate of 10 Hz. The dye laser with a line bandwidth of 0.04 cm^{-1} was tuned to generate an output at a wavelength around 226.263 nm to excite the P1^4 and R2^{11} rotational states of ground state NO molecules, the transition NO X($v'' = 0$) → A($v' = 0$).

The laser wavelength was scanned across the transition to achieve the highest intensity LIF signal thus determining the wavelength at which the maximum ground state NO excitation occurs. Parasitic effects that can affect the LIF signal and therefore require consideration have been identified in recent work.[21] No fluorescence signal was detected from the dielectric surface or in the discharge gap when the plasma was off, indicating that any parasitic effects from spurious laser scattering can be neglected in our analysis. The photoemission of charged species such as NO(A) produced in the discharge was also considered to be unimportant due to the low energy of the laser used in the experiments and the fact that NO excitation is
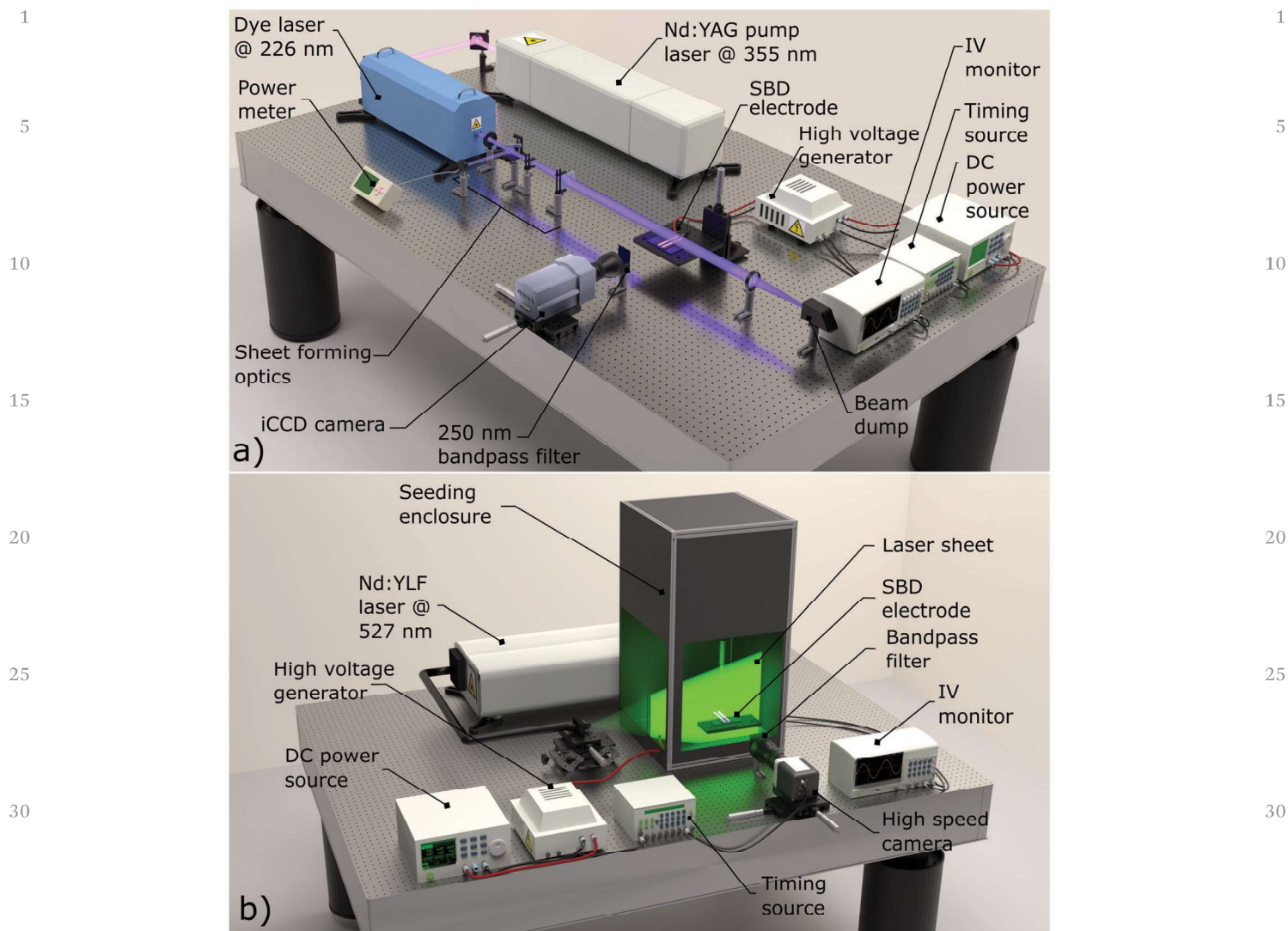
2 | *Phys. Chem. Chem. Phys.*, 2018, **00**, 1–12

This journal is © the Owner Societies 2018

Fig. 2 Schematic showing arrangement of diagnostic apparatus including: (a) laser induced fluorescence system for measurement of ground state NO and (b) particle imaging velocimetry system for measurement of velocity flow fields.

a resonant process. Other possible parasitic effects were tested by shifting the laser wavelength by more than 5 pm away from the centre of the transition at 226.263 nm. Detuning the laser wavelength from the centre of the transition resulted in no ~~fluorescence~~ signal detection, thus other parasitic effects that can disturb the LIF measurements can also be neglected.

The laser pulse energy was monitored in real-time using an Ophir PE-9 laser energy meter and was kept within the range of 0.07–0.1 mJ. Using a cylindrical lens (with 100 mm focal length), the dye laser output was converted into a 13 mm sheet propagating perpendicularly above the discharge. The slight divergence of the laser beam after the cylindrical lens was neglected. To capture the fluorescence of excited NO molecules, an Andor iStar740 iCCD camera was fitted with a UV Nikkor 50 mm imaging lens *via* an optical bandpass filter. The filter had a full width half maximum bandwidth of 10 nm and was used to capture the fluorescence signal at $\sim$248 nm corresponding to the NO transition of $A(\nu'' = 0) \rightarrow X(\nu' = 2)$. The

camera arrangement was positioned to face the centre of the discharge gap between the two driven electrodes. For each image recorded the iCCD camera was configured to accumulatively capture 40 laser pulses, using an optical gate width equal to 30 ns for each exposure. All images of the LIF signal were corrected for background noise and plasma emission prior to analysis of the results. The divergence of the laser sheet was determined to be 15.7 mrad due to the presence of the sheet forming optics; over the camera field of view, this level of divergence was found to be negligible hence no correction of the data was applied.

A calibration procedure described in detail by Van Gessel *et al.*[15,16] was used to convert the fluorescent signal in to the NO number density within the region of interest. To obtain calibration data, an experimental setup with the same optical elements and the same detector position was used with the exception of the SBD being replaced with a sealed chamber filled with ultra-pure helium at pressures of 300, 500, 700, and

This journal is © the Owner Societies 2018

Phys. Chem. Chem. Phys., 2018, **00**, 1–12 | **3**

900 mbar plus an admixture of 100 ppm of NO. Multiple He/NO pressures were used to account for possible reflections from inside the chamber. The LIF signal accumulated by the ICCD camera was corrected for the laser energy, according to eqn (1):[15]

$$I_{\text{LIF}}^{\text{cal}} = \frac{I_{\text{LIF}}^{0}}{E_{\text{L}}\eta_{226}\eta_{248}} \qquad (1)$$

where I_{LIF}^{0} is the LIF signal intensity per pixel measured as an average value over a region of interest, E_{L} is the laser energy while η_{226} and η_{248} are the transparency of the windows of the vacuum chamber used for the laser beam pass and fluorescence signal detection, respectively. Using this parameter, the NO concentration, n_{NO}, in the discharge was calculated using eqn (2):[15,16]

$$n_{\text{NO}} = \frac{I_{\text{LIF}}^{\text{SBD}}}{I_{\text{LIF}}^{\text{cal}}} \frac{\tau_{\text{cal}}}{\tau_{\text{SBD}}} n_{\text{NO}}^{\text{cal}} \qquad (2)$$

where, is the LIF signal measured from the SBD discharge normalised to the laser energy and corrected for O_3 absorption, $n_{\text{NO}}^{\text{cal}}$ is the known density of NO in the calibration mixture, τ_{cal} (s) and τ_{SBD} (s) are the LIF signal (i.e. fluorescence) decay time in the discharge and in the calibration chamber respectively.[15,22–26] The required decay times τ_{SBD} (s) and τ_{cal} (s) were estimated based on known densities of the quenchers (He, N_2, O_2, H_2O, NO, O_3) in the discharge and the calibration cell and known rate coefficients given elsewhere.[15] LIF measurements were conducted for the two power conditions under both steady state and pulsed operation. To achieve steady state conditions, the discharge was energised for tens of seconds prior to measurements being taken. To reveal the spatiotemporal evolution of NO, the applied voltage was modulated with a square wave at a frequency of 10 Hz resulting in the plasma being on for 50 ms and off for 50 ms, with LIF measurements being taken at 5 ms intervals over both the on and off time.

2.3 Particle imaging velocimetry setup

In order to quantify the flow field created by the plasma particle imaging velocimetry (PIV) was used. The PIV technique employs a pulsed laser formed in to a sheet to illuminate fine oil droplets within the measurement domain. A high-speed camera is used to capture one laser pulse per frame and a cross correlation technique is used to track the displacement of particles between consecutive frames. The precise timing between laser pulses and the measured displacement of particles enables velocity vectors in 2D space to be calculated. PIV measurements were undertaken using the experimental setup shown in Fig. 2(b). The SBD was inserted into a large chamber (volume >2 m^3), which was seeded using oil droplets with a nominal size of 1 μm. To prevent any influence on the plasma generated flow from external draughts the chamber was sealed for all measurements. The Stokes number of the seeding particles used throughout the study was <0.1, thus ensuring that the particles followed the fluid flow closely with tracing errors being $<1\%$.[27] A double pulsed Nd:YLF laser operating at 400 Hz with a pulse duration of 100 ns and wavelength of 527 nm was used to generate a light sheet that was projected into the seeding chamber and across the SBD electrode. A high-speed Phantom Miro Lab 340 camera was positioned outside the seeding chamber perpendicularly to the laser sheet and synchronised with the laser such that each frame captured a single laser pulse. A spatial calibration was performed and the time delay between consecutive laser pulses (ΔT) was set to 20 μs, a value chosen to capture the movement of oil droplets over a square grid with spatial resolution of 56 μm, enabling the velocity vectors to be computed using a recursive cross-correlation technique. For each dataset, 800 frames were recorded and used to make 400 individual vector maps; in the case of time averaged measurements all 400 vector maps were averaged and presented as a single figure.

2.4 Numerical model

The main numerical model used in this study was a 2D time dependent reactive flow model, comprising of two modules that each computed the variables necessary for the main model. Fig. 3 indicates how the plasma module and the chemistry module were coupled with the reactive flow model. A detailed description of the full model and its components is given in the ESI.† A brief model description is given here highlighting the key equations and assumptions made.

The plasma module linked experimental parameters, such as the electrode geometry, applied voltage waveform, and dielectric thickness to variables needed by the reactive flow model, these variables were the EHD force field and the plasma power density. The experimental parameters were chosen to exactly match those used in experiments.

In terms of its structure, the plasma module was based on a fluid description of the plasma that was defined only in the discharge gap region indicated in Fig. 1. It included a minimal set of species, as incorporating a large set of species and reactions is computationally prohibitive. The rationale behind this adopted approach was to use the plasma module to accurately capture the physics of the discharge while the chemistry of the discharge was accurately modelled using the
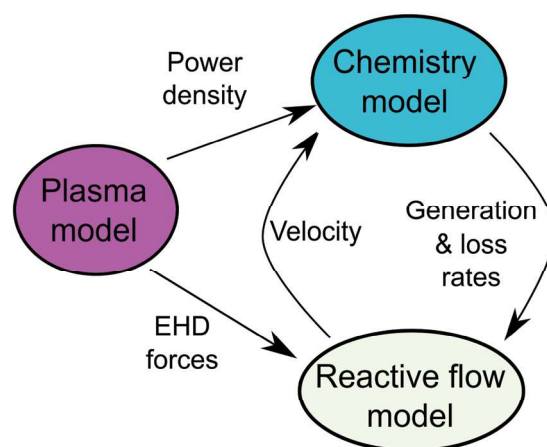

Fig. 3 Diagram showing the coupling between different modules within the computational model.

4 | Phys. Chem. Chem. Phys., 2018, 00, 1–12

This journal is © the Owner Societies 2018

chemistry module described subsequently. The plasma module solved the continuity equation, eqn (3), for the densities of electrons, N_2^+, O_2^+, O_2^-, and the electron energy density.

$$\frac{\partial n_i}{\partial t} + \nabla \cdot (-n_i \mu_i \nabla V - D_i \nabla n_i) = R_i \qquad (3)$$

In eqn (3), n_i is the density of the ith species (m^{-3}), μ_i is the mobility of the ith species (m^2 V^{-1} s^{-1}), V is the electric potential (V), D_i is the diffusion coefficient of the ith species (m^2 s^{-1}). The last term R_i is the rate expression of the ith species where all generation and loss terms are included in that term.

The plasma module also solved the Poisson equation, given by eqn (4), for the electric potential V (V) in the discharge gap and the dielectric. In addition to the equation for the evolution of the surface charge density on the plasma-dielectric interface ρ_s (C m^{-2}), given by eqn (5).

$$\nabla^2 V = \frac{-e}{\varepsilon_0 \varepsilon_r} \left(\sum n_+ - \sum n_- \right) \qquad (4)$$

$$\frac{\partial \rho_s}{\partial t} = e\hat{n} \cdot \left(\sum \vec{\Gamma}_+ - \sum \vec{\Gamma}_- \right) \qquad (5)$$

In eqn (4) and (5), e is the electron charge (C), ε_r is the relative dielectric permittivity (F m^{-1}), which was assumed to be 4.7 in the dielectric and 1 in air, $\hat{n}$ is the normal unit vector on the dielectric surface. The summations $\sum n_+$ and $\sum \Gamma_+$ run over the densities and the fluxes of positively charged species respectively, identically the summations $\sum n_-$ and $\sum \Gamma_-$ run over the densities and the fluxes of negatively charged species respectively.

Further mathematical details of the plasma module, including boundary conditions, list of included reactions, and definition of different parameters are given in the ESI.† Considering that the plasma module was run for one period only (period duration of ∼55.5 μs), it was assumed that convection is ignored on this timescale, and that gas temperature was fixed at room temperature. After the module was solved, the time-averaged EHD force field was exported to the reactive flow model, while the plasma power density as function of time was exported to the chemistry module.

Outputs from the plasma model are passed as inputs to the chemistry module which was based on a 0D global model following 52 species including electrons, ions, excited and neutral species involved in 625 reactions. A full list of the included species and the associated reactions are referred to in the ESI.† The output of the plasma module showed that most of the electron-driven reactions occurred within a small area in the discharge gap next to the electrode and that the reaction rates decayed rapidly away from the small region. These findings were consistent with experimental observations showing the plasma emission, which is known to be primarily driven through electronic excitation, to be confined to a region close to the electrode edges. Based on these findings, the 0D chemistry module was used to describe the chemistry at that location. The power density at the centre of the region was extracted from the

plasma module, then used as input to the chemistry module to make the simulated chemistry consistent with the physical conditions. The chemistry module solved the conservation equation for every species in the module, as given in eqn (6), in addition to an equation for the electron temperature, as given in eqn (7).

$$\frac{\partial n_i}{\partial t} = R_i - \frac{n_i \vec{u}}{d} \qquad (6)$$

$$\frac{\partial}{\partial t} \left(\frac{3}{2} n_e T_e \right) = P_{dep} - S_{en} \qquad (7)$$

In eqn (6) and (7), n_i is the density of the ith species, R_i is the rate expression of the ith species, $\vec{u}$ is the velocity field at the point where the chemistry module is evaluated, which is calculated from the reactive flow model as described later, and d is a characteristic length of the high reactivity region where the chemistry module is defined, n_e is the electron density, T_e is the electron temperature, P_{dep} is the power deposition obtained from the plasma module, and S_{en} is the energy collisional loss computed by the chemistry module.

The chemistry module was solved for 10 periods of the applied voltage waveform, which provided sufficient time for short-lived species to obtain the expected periodic behaviour. In the final period, the effective generation or loss rates of long-lived species due to short lived species were averaged in time, then used as an input to the reactive flow model. An example of this procedure is given in the ESI.† Since the chemistry module was dependant on the reactive flow model *via* the flow velocity, and the reactive flow model was dependant on the chemistry module, *via* generation and loss rates, the two components were solved iteratively as the reactive flow model was run.

The last and the main frame of the overall model was the reactive flow model. The reactive flow model solved for the velocity field of the gas mixture and the concentrations of only the neutral (long-lived) species in the entire computational domain, shown in Fig. 1. In this context, long-lived species are those that are defined as having a lifetime longer than the period of the waveform. To describe the flow, the model required the EHD force field induced by the SBD calculated by the plasma module. Equations solved in the reactive flow model are essentially Navier–Stokes equations for the flow of the gas mixture, coupled to continuity equation for the specie followed in the reactive flow model, as given in eqn (8)–(10).

$$\frac{\partial \rho}{\partial t} + \nabla \cdot \left(\rho \vec{u} \right) = 0 \qquad (8)$$

$$\rho \frac{\partial \vec{u}}{\partial t} + \rho \vec{u} \cdot \nabla \vec{u} = -\nabla P + \zeta \nabla^2 \vec{u} + \vec{F}_{EHD} \qquad (9)$$

$$\frac{\partial n_i}{\partial t} + \nabla \cdot \left(-D_i \nabla n_i + n_i \vec{u} \right) = R_i \qquad (10)$$

In eqn (8)–(10), ρ is the mass density of the species mixture (kg m^{-3}), which was defined in terms of the individual species as $\rho = \sum_k m_k n_k$ such that m_k is the molecular mass (kg) of the

This journal is © the Owner Societies 2018

Phys. Chem. Chem. Phys., 2018, **00**, 1–12 | 5

kth species and n_k is its number density (m^{-3}), $\vec{u}$ is the velocity field (m s^{-1}), ζ is the air's viscosity (Pa s), P is the pressure (Pa), and $\vec{F}_{\text{EHD}}$ is the time-averaged EHD force field obtained from the plasma module, given by eqn (11). All the parameters of eqn (10) were already defined.

$$\vec{F}_{\text{EHD}} = \frac{1}{T} \int_0^T -e\left(\sum n_{+(t)} - \sum n_{-(t)} \right) \nabla V_{(t)} \mathrm{d}t \qquad (11)$$

In eqn (11), T is the period of the waveform (s), and all other parameters were previously defined. The values of the EHD force field ranged from 0 to 5 kN m^{-3}. It should be noted that eqn (11) implicitly implies that the momentum gained by the ions from the electric field is instantly transferred to the neutrals forming the background gas. Considering that the time between two consecutive ion-neutral collision, in the order of $\sim 10^{-10}$ s, is shorter than the timescale of the simulated plasma, this assumption is well justified.

The chemical reactions among the long-lived species were treated explicitly while the chemical reactions between the long-lived and the short-lived species were treated implicitly, using effective generation and loss rates of the long-lived species due to the short-lived species, obtained from the chemistry module. The details of this treatment are given in the ESI.† The term R_i in eqn 10 thus includes both the explicit long-lived species reactions and the implicit short-lived species reactions.

It was assumed in the reactive flow model that the gas temperature was equal to room temperature. Experimental evidence showed that heating became significant after minutes of operation. Considering that the timescales investigated in this work, ranged from milliseconds to seconds, the increase in gas temperature was insignificant and thus ignored. The boundary conditions used in the reactive flow model are listed in the ESI.†

3. Results and discussion

3.1 Temporal evolution of NO generation and transport

To study the spatiotemporal evolution of NO generation and transport from the SBD the discharge was pulse modulated with a period of 100 ms and duty cycle of 50%. During the discharge on-time, the spatial distribution of NO and the EHD induced velocity field were measured in a region that extended 10 mm from the dielectric surface and 1 mm either side of the discharge gap. Fig. 4 shows the temporal evolution of the velocity field from the instant the 13 kV signal was applied to the powered electrodes (0 ms) over the 50 ms on-time and a further 20 ms of the off-time. From the figure it is clear that the flow originates close to the electrodes edges, in the regions where the visible plasma was observed, and is directed toward the opposite electrode. Between 10 and 20 ms the two opposing induced flows coalesce in the centre of the discharge gap and as a result of conservation of momentum the flow is redirected
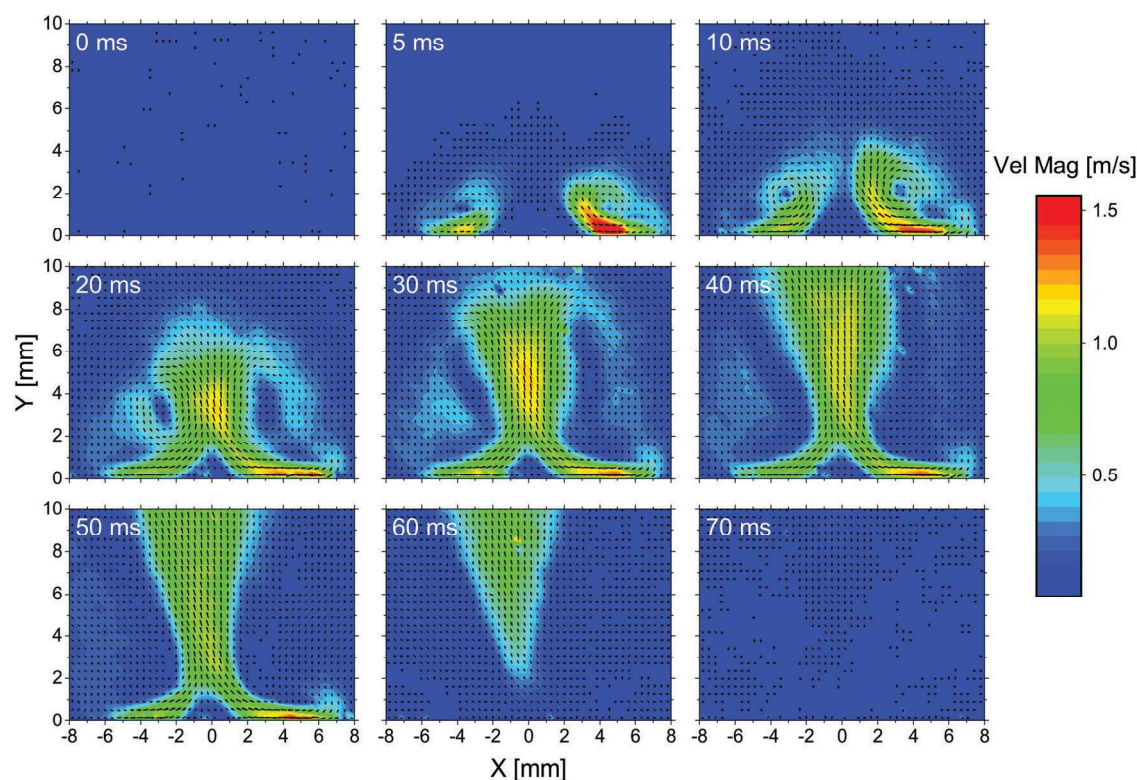

Fig. 4 Temporal evolution of the velocity vector field from the SBD under low power condition (13 kV case) at times, where $t = 0$ is the instant the discharge was energised.

6 | *Phys. Chem. Chem. Phys.,* 2018, **00**, 1–12

This journal is © the Owner Societies 2018

vertically, forming a jet perpendicular to the dielectric surface. The vertical jet was observed to have a narrow width at the point where the two opposing horizontal flows met which expanded as it propagated away from the dielectric surface. After 40 ms the flow was observed to have reached steady state conditions, showing no further changes in spatial profile regardless of operation time; consequently, this profile was considered to represent the steady-state conditions. At 50 ms the applied voltage was terminated and a rapid inhibition of the flow parallel to the dielectric surface, as highlighted at 60 ms, was observed. The sudden termination in flow was attributed to friction forces exerted by the dielectric surface. Within a further 10 ms, no flow was observed within the entire measurement domain. Due to slight irregularities in the construction of the SBD device it can be observed that the right-hand side discharge was slightly more intense compared to the left, creating a higher velocity flow leading to a slightly tilted vertical jet.

NO concentration measured using LIF at time points corresponding to the PIV measurements are shown in Fig. 5. The visible artefact seen to appear on the right side of the image at time frames of 0, 60 & 70 ms was attributed to possible contact of the laser beam with the insulating tape on the solid surface of the electrode system and broadband fluorescence. This reflection of the laser beam cannot affect the NO density map and was excluded in analysis of the results.

Following application of the high voltage signal at 0 ms, it can be seen that the NO concentration within the vicinity of the electrodes rose to approximately 300 ppm within 5 ms. Between 5 ms and 50 ms a close correlation can be observed between the profile of ground state NO density and the spatial profile of the induced gas flow, shown in Fig. 4. As NO molecules are transported vertically away from the dielectric surface the concentration dropped from approximately 300 ppm at the surface to approximately 50 ppm at a distance of 6 mm above the surface. Following termination of the plasma at 50 ms, it can be seen that the NO concentration across the dielectric surface dropped rapidly, while downstream of the dielectric surface several tens of ppm remain. These measurements indicate that the loss rate of NO in the vicinity of the dielectric surface is greater than that downstream, a comprehensive explanation for this observation is provided in section 3.2. Within 20 ms of discharge termination, the NO concentration was observed to drop to approximately zero everywhere within the measurement domain.

Through comparison of Fig. 4 and 5, it is very clear that the NO concentration follows the velocity field at any given time. This observation clearly demonstrates that the induced EHD force and the generation of NO occur at the same position (*i.e.* next to the electrode edges where the visible discharge exists) and some proportion of the generated NO is transported by convection to the centre of the discharge gap and downstream
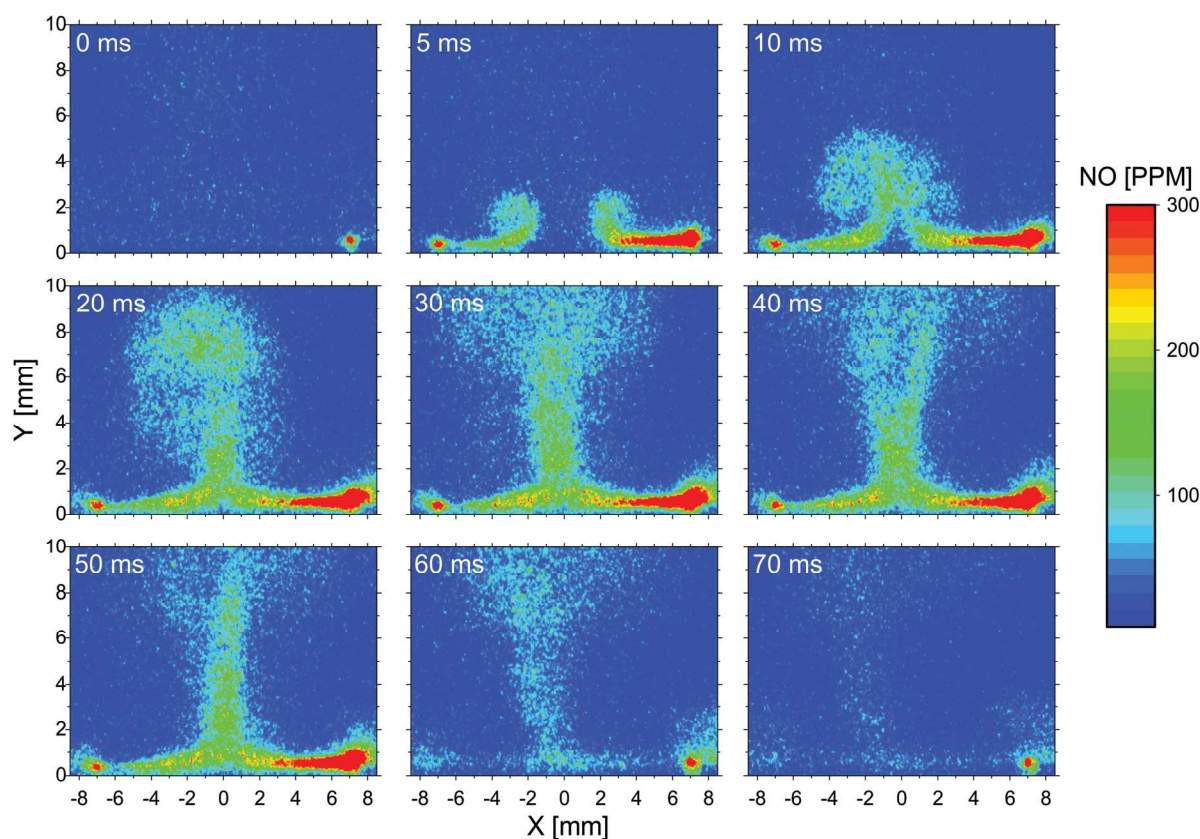

Fig. 5 Temporal evolution of NO density from the SBD under low power conditions at times, where *t* = 0 is the moment the discharge was energised.

along the resultant perpendicular jet. Critically, such observations give credence to the assumptions made in the computational model relating to the generation of reactive species being primarily confined to a small region close to the electrodes edges.

3.2 Comparison of predicted & measured parameters

The computational model was validated by comparing the calculated steady state velocity field and resulting spatial profile of NO to those measured under identical conditions. The discharge was run continuously for a few seconds to ensure

steady state conditions under both applied voltage conditions. Fig. 6 shows the measured and modelled steady state velocity field and NO concentration profile. It is clear that the 2D structure of both the velocity field and NO concentration predicted by the model is highly consistent with measured data. To provide further comparison, both the velocity and concentration data was extracted along a cut line extending from the centre of the discharge gap at the dielectric surface to 10 mm above the surface and plotted in Fig. 6(e) and (f), respectively. The comparison highlights that the calculated parameters are in good qualitative agreement with the
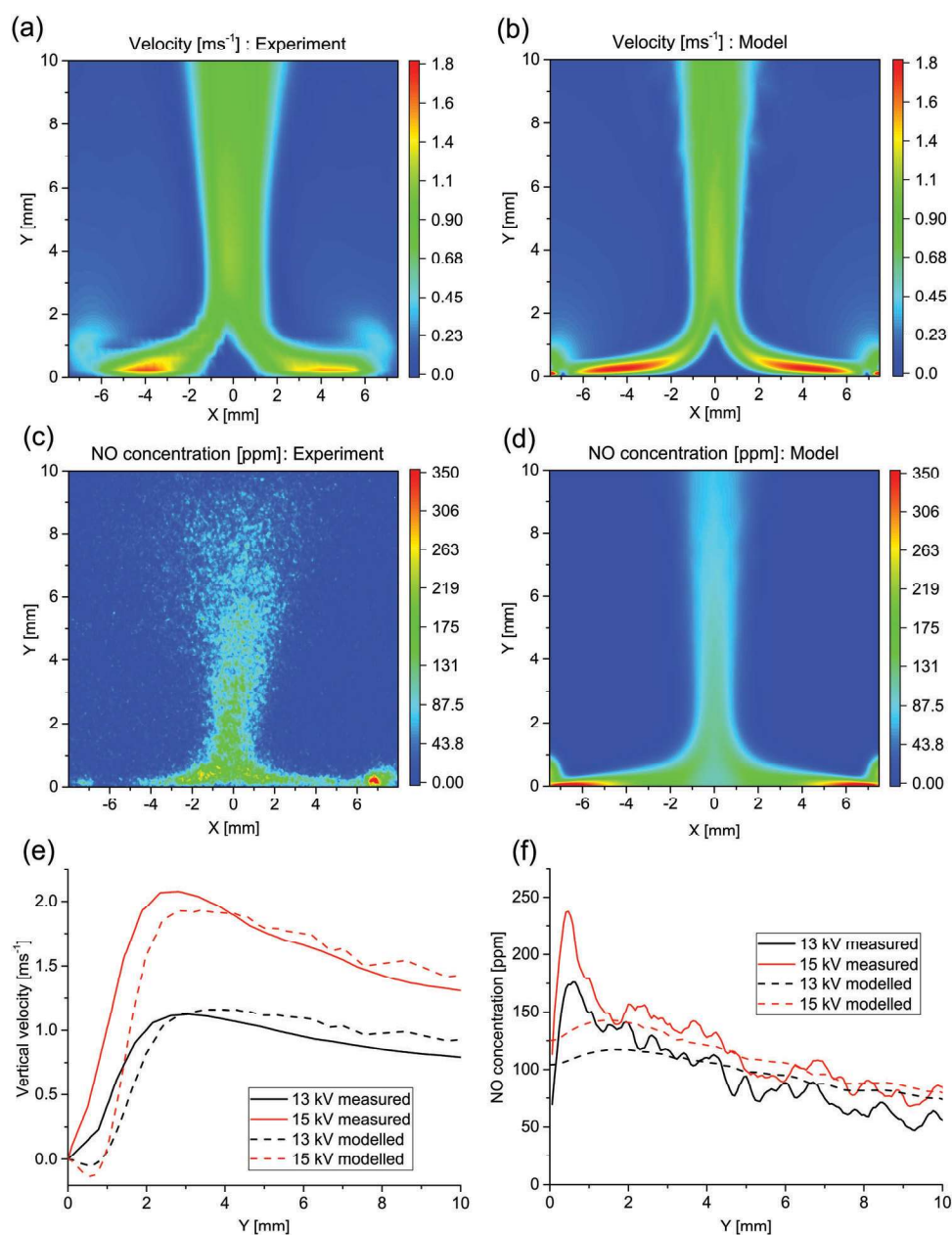

Fig. 6   Steady state velocity profiles at an applied voltage of 13 kV: (a) measured data and (b) modelled data. Steady state NO concentration profiles at an applied voltage of 13 kV: (c) measured data and (d) modelled data. (e) Comparison of measured and modelled velocity along a cut line from the discharge gap centre at applied voltages of 13 and 15 kV. (f) Comparison of the measured and modelled NO concentration along a cut line from the discharge gap centre at applied voltages of 13 and 15 kV.

measured values under both of the discharge conditions considered. While the calculated velocity profile showing excellent agreement with the measured values, the predicted NO concentration appears to be less consistent. Notably, it is clear that the model slightly underestimates the NO concentration, particularly close to the dielectric surface, while the agreement improves in the downstream region. This difference can be attributed to the assumptions made in the model relating to the generation of species at the same point in the discharge region. For different discharge voltages, the trend predicted by the model is consistent with the measured data and it is evident that the model can reliably predict not only the trends, but also the absolute concentrations to within an order of magnitude of the measured data.

3.3 Generation and loss of NO

The model was used to identify the dominant reaction pathways leading to the generation and loss of NO and other key RNS species. Given that reaction rates calculated by the model, as described by eqn (3) in the ESI,† are 2 dimensional; dominant reactions are defined in terms of the overall amount of species existing in the computational domain. The dominant generation mechanism of NO is given by reaction (R1), which describes an effective chemical route in which atomic Oxygen reacts with vibrationally excited N_2, forming NO and atomic nitrogen. Considering that the reaction coefficients describing this chemical pathway do not exist, an effective rate coefficient between atomic oxygen and molecular nitrogen has been fitted in air over a range of pressures and temperatures close to ambient conditions, as described elsewhere.[11,13] The dominant loss mechanism of NO is given by reaction (R2).

$$O + N_2 \rightarrow NO + N \qquad (R1)$$

$$NO + O_3 \rightarrow NO_2 + O_2 \qquad (R2)$$
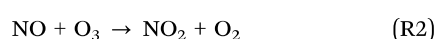
Considering that O and vibrationally excited N_2 only exist in the visible plasma region, close to the electrodes, it can be concluded that this is the only location where NO is actually generated. NO observed beyond this region can only be attributed to transport by the induced flow. On the other hand, as O_3 is relatively stable and spreads significantly beyond the discharge gap,[28] the loss reaction of NO occurs at every point where NO and O_3 coexist. Hence NO is gradually lost as it is transported downstream under the influence of reaction (R2). Based on this insight, it is clear that a combination of the widening of the jet downstream and the loss reaction with ozone are responsible for the decay in the concentration of NO downstream.

Based on these insights, the rapid loss of NO at the dielectric surface identified in Fig. 5 can be explained by two factors, the first is that O_3 highest concentration was found by the model to reach approximately 200 ppm in the vicinity of the dielectric surface, meaning that reaction (R2) plays a comparatively larger role in this region compared to any downstream location, leading to a higher loss rate of NO in the vicinity of the surface. The second factor is the induced flow, which removes NO from

the discharge region to the downstream region. When the applied voltage was increased from 13 kV to 15 kV, the discharge power was increased by a factor of 1.72. This increase in discharge power caused an increase in the induced velocity by a factor of 1.85 at the peak velocity point and a 1.65 increase further downstream. Hence the increase in discharge power caused a proportional increase in the induced velocity field. For the NO concentration, however, the increase in discharge power caused an increase in NO concentration by a factor of 1.37 at the electrode surface and less downstream, as highlighted in Fig. 6(f). The increase in NO concentration is less than the increase in the discharge power or the induced velocity. As described earlier, NO is mainly generated through reaction (R1) which depends on O. The model shows that the O concentration increases by a factor of ~ 1.7, which is proportional to the increase in the discharge power. Given that O is an important precursor for both NO, O_3, and many other species the resulting increase in O concentration is essentially distributed across the spectrum of species created from reactions involving O; thus explaining why the NO concentration only increases by a factor of 1.37, compared to that of 1.72 for the discharge power.

3.4 Generation and loss of other RNS species

It was established in Section 3.2 that the model is able to accurately predict the concentration of NO to within an order of magnitude, it is anticipated that a similar degree of accuracy can be achieved for the many other chemical species produced by the discharge. Under the same experimental conditions as those examined in Section 3.3, the spatial distribution of a further three key RNS species: N, N_2O, and NO_2, were calculated and are depicted in Fig. 7. From Fig. 7(a) it is clear than atomic nitrogen, N, is generated only within the plasma region and that it does not live long enough to be transported downstream by the induced flow. This is due to the high reactivity of N, causing it to be lost through rapid reactions, primarily reaction (R3). Despite the consumption of NO in reaction (R3), it is a relatively minor loss pathway for NO in comparison to reaction (R2).
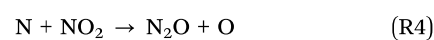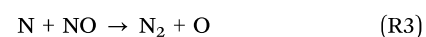
$$N + NO \rightarrow N_2 + O \qquad (R3)$$

$$N + NO_2 \rightarrow N_2O + O \qquad (R4)$$

Fig. 7(b) shows the spatial distribution of N_2O which exhibits clear similarities to the spatial profile of NO, shown in Fig. 6. Critically, N_2O is primarily generated in the discharge region through reaction (R4) and it is inherently stable. Given that its loss rate due to chemical reactions is negligible compared to its generation rate any reduction in N_2O concentration in the downstream jet region can be solely attributed to the widening of the jet and the dispersal of the molecules over a larger volume. Fig. 7(c) shows the spatial distribution of NO_2, similar to N_2O and NO, the concentration of NO_2 reaches a maximum at the centre of the discharge gap and drops as it is transported downstream. NO_2 is mainly generated by reaction (R2) involving both NO and O_3; critically, both of these precursors are present in the induced jet in
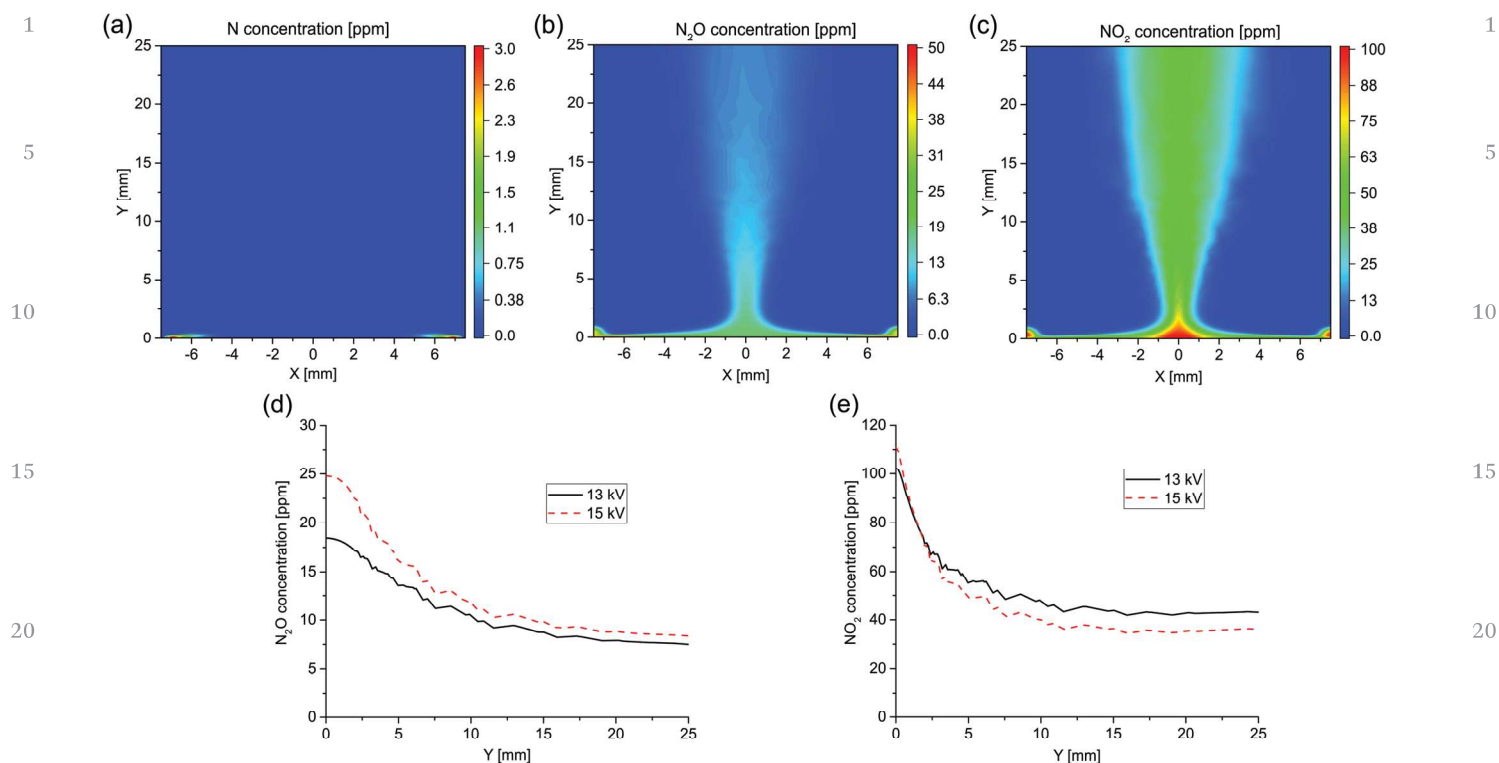
Fig. 7 Calculated spatial distribution of: (a) N, (b) N_2O and (c) NO_2 at an applied voltage of 13 kV. Predicted centre line density profiles of (d) N_2O and (e) NO_2 for applied voltages of 13 and 15 kV.

high concentrations meaning NO_2 is generated in the downstream jet region, away from the discharge. It can be observed that the generation rate of NO_2 downstream counteracts the effect of the widening jet meaning the concentration reduces very slowly as the jet broadens.

The influence of increasing the applied voltage on N_2O and NO_2 concentration is highlighted in Fig. 7(d) and (e), respectively. Similar to NO, the change in concentration of both species is not proportional to the change in the discharge power. This is attributed to both species having at least one precursor species that only depend on the discharge power indirectly, hence the increase in the discharge power is "dissipated" into many cascade reactions leading to the formation of N_2O and NO_2. It is noticeable that the NO_2 concentration decreases in the downstream region as the discharge power is increased, this occurs as a result of the competition between the widening jet and the further generation of NO_2, reaction (R1). An increase in discharge power causes a proportional increase in the flow velocity of the induced jet, while the increase in the generation reaction rate does not increase sufficiently to balance the loss, leading to a shift toward a lower NO_2 concentration in the downstream region.

4. Conclusions

The reaction pathways and transport mechanisms of key reactive nitrogen species produced by a surface barrier discharge operating in open air were examined using computational modelling and experimental measurements. Particle imaging velocimetry was used to uncover the induced flow structure created by electrohydrodynamic forces generated by the plasma while laser induced fluorescence was used to obtain ~~measurements of~~ ground state NO density. Both techniques facilitated time and space resolved measurements and were applied to analyse the discharge under two different applied voltage conditions. Steady state measurements of the discharge were used to benchmark the developed numerical model, which was then used to identify the main reaction pathways and predict the behaviour of other reactive nitrogen species.

It was shown that the induced velocity and source of NO both originated at the edge of the driven electrodes which corresponded to the visible plasma region; beyond this region the NO concentration was seen to extend into the centre of the discharge gap and vertically away from the dielectric surface in the form of a perpendicular jet, closely mirroring the measured velocity profile. Along the axis of the induced vertical jet, steady state measurements showed that the NO concentration peaked at the dielectric surface and then dropped downstream. Using the numerical model it was found that NO is generated through an effective reaction pathway involving vibrationally excited N_2 and atomic oxygen. While the dominant loss reaction of NO was found to be with O_3, creating NO_2. Since both NO and O_3 are transported by the induced flow, the decay reaction contributes to a drop in NO concentration in the downstream region.

In addition to capturing the spatiotemporal behaviour of NO, the model was used to predict the 2D distribution of N, N_2O, and NO_2. It was shown that N is entirely restricted to a region near the electrodes, where it is generated through electron driven dissociation and rapidly consumed by reactions leading to the formation of N_2 and O. The spatial profiles of both N_2O and NO_2 were seen to be similar to NO in that they appeared to follow the induced flow; however, unlike NO and N_2O, NO_2 was found to be created downstream by a reaction involving NO with O_3.

The effect of increasing the discharge power was also investigated and it was shown that the resulting increase in velocity is proportional to the increase in discharge power, while the change in the concentrations of NO, N_2O, and NO_2 does not follow the same trend. This phenomenon occurs because these species are indirectly influenced by the discharge power through a sequence of cascade reactions involving species such as O, which are directly influenced by the discharge power. As the respective increase in the flow velocity is larger than the respective increase in NO and O_3 concentration, which are the precursors of NO_2, increasing the discharge power leads to a drop in the concertation of NO_2, while NO and N_2O concentrations increase as the discharge power is increased.

Overall, this study highlights that significant densities of reactive nitrogen species can be delivered significant distances downstream of a surface barrier discharge. Notably NO, which is of considerable biological importance and a key application enabler, was observed to be transported several centimetres downstream of the discharge region by the plasma induced flow. Through computational modelling the key reaction pathways responsible for the generation and loss of major reactive nitrogen species have been identified and this insight can be used to aid in the development and understanding of plasma-based healthcare devices employing the surface barrier discharge configuration.

Conflicts of interest

There are no conflicts to declare.

Acknowledgements

References

1 M. Modic, N. P. McLeod, J. M. Sutton and J. L. Walsh, Cold atmospheric pressure plasma elimination of clinically important single- and mixed-species biofilms, *Int. J. Antimicrob. Agents*, 2017, **49**(3), 375–378, DOI: 10.1016/j.ijantimicag.2016.11.022.

2 S. Kubinova, K. Zaviskova, L. Uherkova, V. Zablotskii, O. Churpita and O. Lunov, *et al.*, Non-thermal air plasma promotes the healing of acute skin wounds in rats, *Sci. Rep.*, 2017, **7**(March), 1–11, DOI: 10.1038/srep45183.

3 J. Liebmann, J. Scherer, N. Bibinov, P. Rajasekaran, R. Kovacs and R. Gesche, *et al.*, Biological effects of nitric oxide generated by an atmospheric pressure gas-plasma on human skin cells, *Nitric Oxide*, 2011, **24**(1), 8–16, DOI: 10.1016/j.niox.2010.09.005.

4 K. Heuer, M. A. Hoffmanns, E. Demir, S. Baldus, C. M. Volkmar and M. Röhle, *et al.*, The topical use of non-thermal dielectric barrier discharge (DBD): Nitric oxide related effects on human skin, *Nitric Oxide*, 2015, **44**(1), 52–60, DOI: 10.1016/j.niox.2014.11.015.

5 B. Haertel, T. von Woedtke, K. D. Weltmann and U. Lindequist, Non-thermal atmospheric-pressure plasma possible application in wound healing, *Biomol. Ther.*, 2014, **22**(6), 477–490, DOI: 10.4062/biomolther.2014.105.

6 F. Vatansever, W. C. M. A. de Melo, P. Avci, D. Vecchio, M. Sadasivam and A. Gupta, *et al.*, Antimicrobial strategies centered around reactive oxygen species – bactericidal antibiotics, photodynamic therapy, and beyond, *FEMS Microbiol. Rev.*, 2013, **37**(6), 955–989, DOI: 10.1111/1574-6976.12026.

7 Y. Gorbanev, C. C. W. Verlackt, S. Tinck, E. Tuenter, K. Foubert and P. Cos, *et al.*, Combining experimental and modelling approaches to study the sources of reactive species induced in water by the COST RF plasma jet, *Phys. Chem. Chem. Phys.*, 2018, **20**(4), 2797–2808, DOI: 10.1039/C7CP07616A.

8 Z. Machala and D. B. Graves, Frugal Biotech Applications of Low-Temperature Plasma, *Trends Biotechnol.*, 2018, **36**(6), 579–581, DOI: 10.1016/j.tibtech.2017.07.013.

9 S. Park, U. Cvelbar, W. Choe and S. Y. Moon, The creation of electric wind due to the electrohydrodynamic force, *Nat. Commun.*, 2018, **9**(1), 371, DOI: 10.1038/s41467-017-02766-9.

10 G. E. Morfill, T. Shimizu, B. Steffes and H. U. Schmidt, Nosocomial infections – A new approach towards preventive medicine using plasmas, *New J. Phys.*, 2009, **11**, 115019, DOI: 10.1088/1367-2630/11/11/115019.

11 T. Shimizu, Y. Sakiyama, D. B. Graves, J. L. Zimmermann and G. E. Morfill, The dynamics of ozone generation and mode transition in air surface micro-discharge plasma at atmospheric pressure, *New J. Phys.*, 2012, **14**(10), 103028, DOI: 10.1088/1367-2630/14/10/103028.

12 M. J. Pavlovich, D. S. Clark and D. B. Graves, Quantification of air plasma chemistry for surface disinfection, *Plasma Sources Sci. Technol.*, 2014, **23**(6), 065036, DOI: 10.1088/0963-0252/23/6/065036.

13 R. Bansemer, A. Schmidt-Bleker, U. Van Rienen and K.-D. Weltmann, Investigation and control of the O_3- to NO-transition in a novel sub-atmospheric pressure dielectric barrier discharge, *Plasma Sources Sci. Technol.*, 2017, **26**(6), DOI: 10.1088/1361-6595/aa6c34.

Q2

This journal is © the Owner Societies 2018

Phys. Chem. Chem. Phys., 2018, **00**, 1–12 | 11

14 K. Takeda, K. Ishikawa, H. Tanaka, M. Sekine and M. Hori, Spatial distributions of O, N, NO, OH and vacuum ultraviolet light along gas flow direction in an AC-excited atmospheric pressure Ar plasma jet generated in open air, *J. Phys. D: Appl. Phys.*, 2017, **50**(19), 195202, DOI: 10.1088/1361-6463/aa6555.

15 A. F. H. Van Gessel, B. Hrycak, M. Jasiński, J. Mizeraczyk, J. J. A. M. Van Der Mullen and P. J. Bruggeman, Temperature and NO density measurements by LIF and OES on an atmospheric pressure plasma jet, *J. Phys. D: Appl. Phys.*, 2013, **46**(9), 095201, DOI: 10.1088/0022-3727/46/9/095201.

16 A. F. H. Van Gessel, K. M. J. Alards and P. J. Bruggeman, NO production in an RF plasma jet at atmospheric pressure, *J. Phys. D: Appl. Phys.*, 2013, **46**(26), 265202, DOI: 10.1088/0022-3727/46/26/265202.

17 A. F. H. Van Gessel, B. Hrycak, M. Jasiński, J. Mizeraczyk, J. J. A. M. Van Der Mullen and P. J. Bruggeman, Temperature fitting of partially resolved rotational spectra, *J. Instrum.*, 2012, **7**(2), C02054, DOI: 10.1088/1748-0221/7/02/C02054%0A.

18 S. Yonemori and R. Ono, Effect of discharge polarity on the propagation of atmospheric-pressure helium plasma jets and the densities of OH, NO, and O radicals, *Biointerphases*, 2015, **10**(2), 029514, DOI: 10.1116/1.4919709.

19 A. Dickenson, Y. Morabit, M. I. Hasan and J. L. Walsh, Directional mass transport in an atmospheric pressure surface barrier discharge, *Sci. Rep.*, 2017, **7**(1), 1–9, DOI: 10.1038/s41598-017-14117-1.

20 M. I. Hasan, Y. Morabit, A. Dickenson and J. L. Walsh, Impact of electrode geometry on an atmospheric pressure surface barrier discharge, *Appl. Phys. Lett.*, 2017, **110**(26), 1–5, DOI: 10.1063/1.4985030.

21 V. Procházka, Z. Tučeková, P. Dvořák, D. Kováčik, P. Slavíček and A. Zahoranová, *et al.*, Coplanar surface barrier discharge ignited in water vapor – A selective source of OH radicals proved by (TA)LIF measurement, *Plasma Sources Sci. Technol.*, 2018, **27**(1), 015001, DOI: 10.1088/1361-6595/aa9ad4%0A%0A.

22 J. B. Nee, C. Y. Juan, J. Y. Hsu, J. C. Yang and W. J. Chen, The electronic quenching rates of NO (A2Σ+, v' = 0–2), *Chem. Phys.*, 2004, **300**(1–3), 85–92, DOI: 10.1016/j.chemphys.2004.01.014%0A%0A.

23 I. J. Wysong, Vibrational energy transfer of NO (NO (X2Π, v = 2 and 1)), *J. Chem. Phys.*, 1994, **101**(4), 2800, DOI: 10.1063/1.467595%0A%0A.

24 T. B. Settersten, B. D. Patterson and J. A. Gray, Temperature- and species-dependent quenching of NO A 2Sigma + (v' = 0) probed by two-photon laser-induced fluorescence using a picosecond laser, *J. Chem. Phys.*, 2006, **124**(23), 234308, DOI: 10.1063/1.2206783.

25 J. Malicet, D. Daumont, J. Charbonnier, C. Parisse, A. Chakir and J. Brion, Ozone UV spectroscopy. II. Absorption cross-sections and temperature dependence, *J. Atmos. Chem.*, 1995, **21**(3), 263–273, DOI: 10.1007/BF00696758%0A%0A%0A.

26 M. C. Drake and J. W. Ratcliffe, High temperature quenching cross sections for nitric oxide laser-induced fluorescence measurements, *J. Chem. Phys.*, 1993, **98**(5), 3850, DOI: 10.1063/1.465047%0A%0A%0A.

27 R. D. Whalley and J. L. Walsh, Turbulent jet flow generated downstream of a low temperature dielectric barrier atmospheric pressure plasma device, *Sci. Rep.*, 2016, **6**(July), 1–7, DOI: 10.1038/srep31756.

28 N. Mastanaiah, P. Banerjee, J. A. Johnson and S. Roy, Examining the role of ozone in surface plasma sterilization using dielectric barrier discharge (DBD) plasma, *Plasma Processes Polym.*, 2013, **10**(12), 1120–1133, DOI: 10.1002/ppap.201300108%0A%0A%0A.

12 | *Phys. Chem. Chem. Phys.*, 2018, **00**, 1–12

This journal is © the Owner Societies 2018